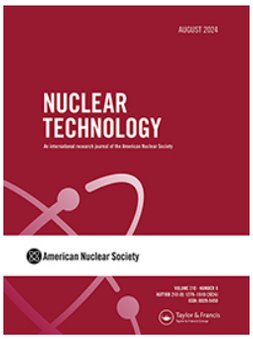

Nuclear Technology

ISSN: (Print) (Online) Journal homepage: www.tandfonline.com/journals/unct20

Analysis of the Long-Term Interaction Between Molten Core and Dry Concrete at Fukushima Daiichi Unit 1

Marco Pellegrini, Christophe Journeau, Nathalie Seiler, Luis E. Herranz, M. García, Claus Spengler, Charlaine Bouillet, Marc Barrachin, David Luxat & Lucas Albright

To cite this article: Marco Pellegrini, Christophe Journeau, Nathalie Seiler, Luis E. Herranz, M. García, Claus Spengler, Charlaine Bouillet, Marc Barrachin, David Luxat & Lucas Albright (24 Jul 2024): Analysis of the Long-Term Interaction Between Molten Core and Dry Concrete at Fukushima Daiichi Unit 1, Nuclear Technology, DOI: 10.1080/00295450.2024.2371267

To link to this article: https://doi.org/10.1080/00295450.2024.2371267

Published online: 24 Jul 2024.

NUCLEAR TECHNOLOGY

DOI: https://doi.org/10.1080/00295450.2024.2371267

Analysis of the Long-Term Interaction Between Molten Core and Dry Concrete at Fukushima Daiichi Unit 1

Marco Pellegrini,[a]* Christophe Journeau,[b] Nathalie Seiler,[b] Luis E. Herranz,[c] M. García,[c] Claus Spengler,[d] Charlaine Bouillet,[e] Marc Barrachin,[e] David Luxat,[f] and Lucas Albright[f]

[a]*The University of Tokyo, Nuclear Professional School, Minatoku, Japan*
[b]*CEA, IRESNE, DTN, SMTA, Cadarache, France*
[c]*CIEMAT, Madrid, Spain*
[d]*Gesellschaft für Anlagen- und Reaktorsicherheit (GRS) gGmbH, Germany*
[e]*Institut de Radioprotection et de sûreté Nucléaire (IRSN), France*
[f]*Sandia National Laboratories, Severe Accident Department, Albuquerque, New Mexico*

Received April 2, 2024
Accepted for Publication June 13, 2024

Abstract — *The latest investigations of Fukushima Daiichi Unit 1 have demonstrated that corium attack to the pedestal walls and pedestal floor has occurred in Fukushima Daiichi Unit 1 to a certain extent. The results of past analytical benchmarks, such as the Organisation for Economic Co-operation and Development (OECD)/Nuclear Energy Agency (NEA) Benchmark Study of the Accident at the Fukushima Daiichi Nuclear Power Plant (BSAF project), have agreed with this finding. However, the latest investigation does not show evidence of unlimited molten core–concrete interaction (MCCI), which is one of the main discrepancies from the BSAF project.*

More recently a MCCI benchmark has been launched in the context of the OECD/NEA project ARC-F (Analysis of Information from Reactor Building and Containment Vessels of Fukushima Daiichi Nuclear Power Station). In the benchmark, common geometry, boundary, and initial conditions have been selected among all the participants. The results show an improved agreement among different codes for what concerns overall erosion, corium temperature, and hydrogen generation, confirming that to some extent, the earlier scatter found in these variables came from differences in the MCCI scenario modeled by each partner.

However, common unlimited erosion, not observed by onsite visual inspections, is still predicted. Understanding the origin of this deviation might provide insights into boundary conditions, model drawbacks, or ill-posed assumptions that might need to be revisited (e.g. interfacial temperature, effective heat transfer coefficients, concrete heat transfer). In this paper, a summary of the overall results and a discussion of modeling and boundary conditions is presented to disclose the results of the activity and the future steps to be taken in the OECD/NEA project FACE (Fukushima Daiichi Nuclear Power Station Accident Information Collection and Evaluation).

Keywords — *Fukushima Daiichi, MCCI, corium, concrete, benchmark, OECD/NEA ARC-F.*

Note — *Some figures may be in color only in the electronic version.*

I. INTRODUCTION

It has been over 13 years since the accident occurred at the Fukushima Daiichi Nuclear Power Station. Since then, analyses of the accident have multiplied, and have been performed in a variety of analytical, experimental, and computational ways. The legacy work of computational analysis of the accident using severe accident (SA) codes is represented by the Organisation for Economic Co-operation and Development (OECD)/Nuclear Energy

*E-mail: marco@n.t.u-tokyo.ac.jp

Agency (NEA) Benchmark Study of the Accident at Fukushima Daiichi Nuclear Power Station (BSAF) phase 1 and phase 2.[1–4]

The project highlighted uncertainties concerning the timing and magnitude of key events, such as containment failure events, core relocation events in the reactor pressure vessel (RPV), RPV rupture events, and corium relocation events onto the cavity floor.[1] During phase 2, several uncertainties that remained concerning fission product (FP) behavior were extensively covered by the activity.

One striking result of both BSAF phases was the extensive progression of molten core–concrete interaction (MCCI) for most of the codes, with unlimited erosion until 500 h, which was not confirmed by any evidence at the damaged nuclear plant.

Indeed, recent inspections (in February 2022,[5,6] March 2022,[7] May 2022,[8] and April 2023[9]) of the Fukushima Daiichi primary containment vessel (PCV) in Unit 1 have provided the latest direct evidence that the overall MCCI progression represents a prediction error. The final shape of the eroded cavity might therefore appear different from that estimated by SA codes. The inspection has also introduced additional points of reflection not considered in the past, for example, the creation of layers of debris outside the pedestal and the identification of large areas where the concrete disintegrated while the rebar remains relatively intact.

In a subsequent project of the OECD/NEA, named Analysis of Information from Reactor Buildings and Containment Vessels of Fukushima Daiichi Nuclear Power Station (ARC-F), some of the issues identified in the BSAF project were further investigated by subgroups free to organize activities to clarify outstanding issues. In particular, group 3 of the ARC-F was dedicated to the MCCI analysis targeting the issue of unlimited concrete erosion predicted by SA codes. Group 3 included seven organizations, namely, Commissariat à l'Energie Atomique (CEA), Centre for Energy, Environmental and Technological Research (CIEMAT), Gesellschaft für Anlagen- und Reaktorsicherheit (GRS), Institute of Applied Energy (IAE), Institute for Radiation Protection and Nuclear Safety (IRSN), Japan Nuclear Regulatory Authority (NRA), and Sandia National Laboratories (SNL), all of which had previously participated in the BSAF project. The group was led by the University of Tokyo.

The focus has on dry MCCI, as very little water is considered to have effectively reached the pedestal floor during the first 10 to 11 days of MCCI.[2] The activity was organized similarly to what was done for the in-vessel degradation, in-depth investigation between the MAAP and MELCOR codes, named Crosswalk.[10]

Namely, geometry, boundary, and initial conditions were agreed on by all the participants and evaluated based on existing data or previous analyses of the BSAF project. In this exercise, the realistic evolution of removed power at the top boundary, which represents the only energy loss, was fixed for all computations. Primary simulation results on concrete vertical and radial erosion and debris temperature were compared, as well as secondary results represented by heat fluxes from the debris (e.g., radiation, convection), which were considered necessary for a thorough evaluation of the computations. The modeling of the heat transfer network was investigated between different codes in order to highlight differences in the erosion pattern.

II. SUMMARY OF BSAF PHASE 2 MCCI PROGRESSION (UNIT 1)

The results of the vertical and lateral erosion for BSAF phase 2 are shown in Fig. 1 and discussed in detail in Refs. [2,11,12]. The vertical erosion shows an unlimited trend for all calculations. Differences in the onset and extent of erosion reflect differences in the timing of RPV failure and total discharged mass, which are presented in Table I. The lateral erosion shows the same trend for all the calculations. Those with flat behavior did not calculate lateral erosion and should not be taken into consideration.

In addition, all codes, except TOLBIAC-ICB, showed a negligible effect of the water injection when erosion continued beyond 270 h, up to 500 h, when alternative water injection became effective.

In the activity proposed for group 3 of the ARC-F, it was decided to evaluate the codes' response to a simplified geometry (i.e., one single sump) with controlled initial and boundary conditions in a dry MCCI progression (i.e., no water injection). The objective of the activity was to confirm the general tendency of the codes to compute an unlimited concrete erosion and identify the main models and parameters responsible.

III. ARC-F GROUP 3 SPECIFICATIONS

III.A. Geometry

The geometry decided for the benchmark was one of the two sumps existing in the pedestal. Sumps are used to accumulate water dripping from the lower head during normal operation. Heat exchangers exist in the sump to

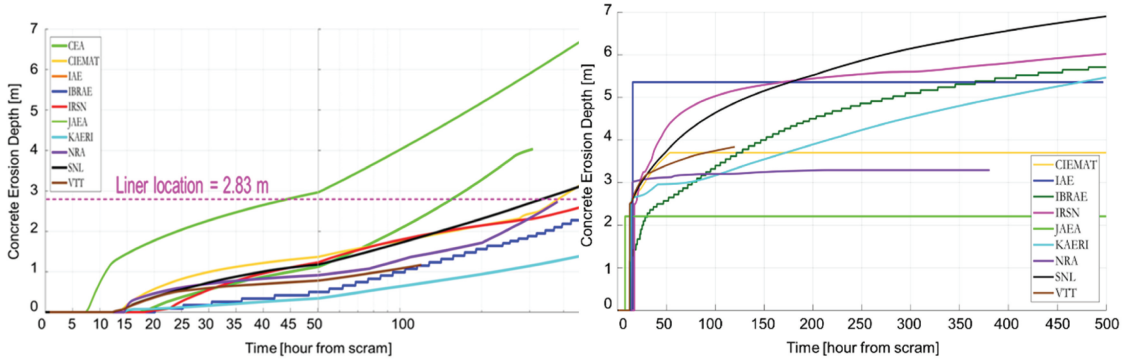

Fig. 1. BSAF phase 2 results for the MCCI vertical erosion for Unit 1: (a) vertical and (b) lateral, where the time axis is presented in logarithmic scale.

cool down the accumulated water. Sumps are considered as the main source of MCCI since the large volume-to-surface ratio generates larger heat fluxes, and thus, are more difficult to cool than the thinner MCCI layer over the pedestal basemat. The dimensions of the sump are reported in Fig. 2. The debris is injected in the middle of the sump. If one of the codes accounted for debris swelling due to gas generation, it was allowed to increase the height of the sump sufficiently to avoid debris overflow.

III.B. Boundary and Initial Conditions

The calculation was assumed to start at time 12.5 h after scram with instantaneous debris injection at this time. The problem was simulated until 270 h after scram without any water injection. No stratification was assumed in the debris. The cavity pressure was assumed equal to 0.7 MPa, and the surrounding gas temperature was assumed to be equal to 438.0 K and composed of inert cases, such as nitrogen.

III.B.1. Initial Debris Composition

The initial mass and composition of the debris were fundamental to defining the amount of oxidation that took place in the MCCI calculations and the overall properties of the corium. The initial composition depended on the history of the core degradation; hence, it was not known. In addition, the composition of the stainless steel and its oxide form were fundamental to controlling the oxidation processes and not known a priori. In the benchmark, it was agreed to employ the characteristics of the degraded state obtained with SNL's MELCOR code in the analysis of Unit 1 during BSAF phase 2[2] as being representative of a plausible accident scenario. These corium and stainless steel (and their oxides) compositions are presented in Tables II and III.

The initial temperature of the debris was assumed following the SNL data as 1481.346 K. Based on its overall composition, the corium density was evaluated as 7647.3 kg/m^3.

III.B.2. Initial Concrete Composition and Properties

The initial composition of the concrete of Fukushima Daiichi was investigated by local inspections after the accident and reported by the Japan Atomic Energy Agency (JAEA) and CEA as in Table IV. As reported, the concrete in Fukushima Daiichi is of basaltic composition. Basaltic concrete, as well as other siliceous concretes, does not contain calcium carbonate; hence, during the degradation and decomposition, only water, in the form of steam, is released in a gaseous form. Metals can eventually be oxidized by gaseous steam to generate hydrogen.

Even though uncertainties still remain, this characteristic of siliceous concretes might create a preferential lateral rather than vertical erosion, which could harm the structures in the containment, such as the one of the Mark I reactor type with a narrow pedestal holding the pressure vessel.[13] This aspect remains unclear, however, as reported in the Vulcano VF-U1 MCCI test[19] performed with this concrete, which showed a preferential vertical ablation.[20] For this reason, to simplify the comparison, isotropic erosion was first considered in the analysis.

The evaluation of the rebar content was more complicated, as this value changes depending on the location

TABLE I

RPV Failure Time and Total Initial Debris Mass in Pedestal of Unit 1*

	CEA[a]	CIEMAT	IAE	IBRAE[b]	IRSN[c]	JAEA	Korea Atomic Energy Research Institute	NRA[d]	SNL	VTT[e]
RPV failure (h)	N/A[f]	11.58	14.97	15.10	17.16	7.45	13.50	13.6	12.5	11.42
Total masses in pedestal (ton)	39	129	148	196	282	130	136	115	154	111

*Reference [26].
[a]This value includes only the debris mass in two sumps since the CEA calculation with TOLBIAC-ICB considered only the sumps. It does not consider the mass above the pedestal and the dry well floor.
[b]IBRAE = Nuclear Safety Institute of the Russian Academy of Sciences.
[c]IRSN shows a larger mass because its results also include a mass of structures belonging to the lower plenum (e.g., control rod guide tubes and the vessel itself).
[d]The NRA total mass in the pedestal does not include stainless steel and stainless steel oxide.
[e]VTT = "Valtion Teknillinen Tutkimuskeskus," Technical Research Center of Finland.
[f]N/A = not available.

in the pedestal. Indeed, some structures are more reinforced than others. An evaluation was done by NRA, and a value of 3.8% based on weight was selected as an average value, while the range of reinforcement was estimated to be between 1.0% to 12.0%. The concrete ablation temperature and energy were evaluated by IRSN based on the concrete composition reported previously. The ablation temperature was evaluated as 1541.0 K and the ablation energy as 1779 kJ/kg using the thermodynamic NUCLEA database.[20]

Even if the ablation concept is a simplification from the point of view of physics, it is usually defined as the process at the concrete interface in which the decomposition products of concrete become incorporated into the core melt or debris. It is expected that this process is characterized by a temperature at which material detaches from the concrete surface. In our evaluation, the ablation energy represents the total heat that is necessary to bring concrete from room temperature to 1541 K (at which 50% of the concrete volume is liquid). The initial concrete temperature was assumed to be 300 K. Concrete density was assumed in all calculations to be equal to 2400 kg/m^3.

III.B.3. Decay Heat

Decay heat must account for the mass of volatile FPs that were released from the fuel during heat up, mostly noble gases, cesium, and iodine. As the released amount is hard to evaluate analytically, the data computed during the BSAF phase 2 project by SNL were taken as reference. SNL provided the total decay heat in the pedestal, which was normalized depending on the mass of debris contained in a single sump. The values are reported in Fig. 3.

III.B.4. Power Loss at the Top Surface

To make sure that boundary conditions were exactly the same for all the codes, it was decided to also impose the top boundary heat loss. As every code considers the contribution for the top heat loss differently (a combination of radiation and convection), it was not possible to fix the physical parameters, such as the surrounding temperature and emissivity. This curve was estimated by SNL based on its previous BSAF analyses.

The heat loss curve is presented in Fig. 3 in comparison with the decay heat, and it shows that the imposed heat loss is always smaller than the decay heat. Even though this approach is ideally the most appropriate, it can create too many constraints for the models, hence in

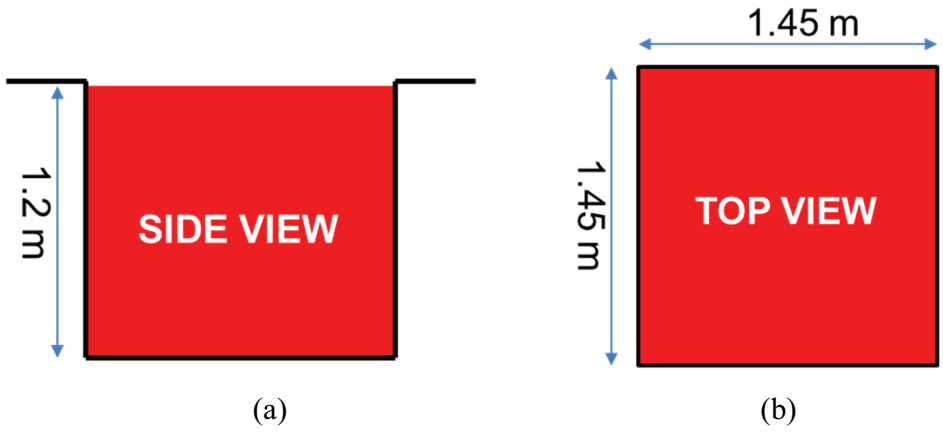

Fig. 2. Geometry to be studied in the ARC-F benchmark by group 3: (a) side view and (b) top view.

future phases of the activities more physics-based boundary conditions will be applied.

TABLE II

Debris Mass Composition Employed in the ARC-F Group 3 Benchmark

Component	Mass (kg)
Stainless steel	5380.60
Stainless steel oxide	458.63
Zr	2106.67
ZrO_2	2356.24
UO_2	9222.18
Total	19524.32

TABLE III

Stainless Steel and Stainless Steel Oxide Compositions Employed in the ARC-F Group 3 Benchmark

	Element	Mass (kg)	Percent
Stainless steel	Cr	1100.00	20.4%
	Ni	471.70	8.8%
	Fe	3808.90	70.8%
Stainless steel oxide	FeO	363.60	79.3%
	Cr_2O_3	47.52	10.4%
	NiO	47.52	10.4%

IV. DETAILS OF THE CODE MODELING

IV.A. Heat Transfer Network

The codes employed by the participants in the exercise are presented in Table V. The main quantities governing heat transfer from the corium pool to the concrete, and hence its erosion, are the temperature of the corium pool T_{melt} and the ablation temperature T_{abl}, which was fixed in our problem (see Sec. III.B.2). The codes can be divided into those that do not consider the crust formation at the corium/concrete interface and those that take it into account, as reported in Table V. Codes in the first group, such as ASTEC/MEDICIS, assume that the convective heat transfer coefficient (HTC) from the corium pool to the concrete is governed by the BALI correlation,[21,22] which reads

$$h_{conv} = 20.5\lambda \left[\frac{\sigma}{(\rho_l - \rho_g)g}\right]^{-0.5} \left[\rho J_g{}^3/\mu g\right]^{0.105} \left[\mu c_p/\lambda\right]^{-0.25}, \quad (1)$$

where

h = convective HTC between the corium pool and the concrete (W/m^2·K)

λ = corium conductive HTC (W/m·K)

TABLE IV

Fukushima Daiichi Unit 1 Concrete Composition

Compound	Al_2O_3	CaO	SiO_2	H_2O	Fe_2O_3
Weight (%)	15.4%	12.8%	62.5%	3.3%	6.0%

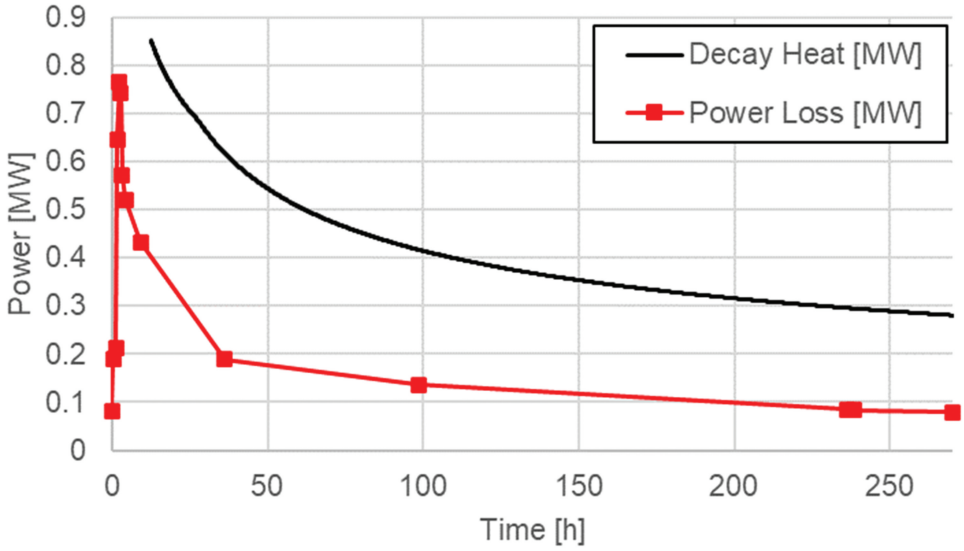

Fig. 3. Decay heat and top boundary power loss imposed in the simulation.

σ = corium surface tension (N/m)

ρ_l = corium density (kg/m^3)

ρ_g = gas density (kg/m^3)

g = gravitational acceleration (m/s^2)

J_g = gas superficial velocity, which accounts for the gas due to the total ablation (bottom and side) (m/s)

μ = dynamic viscosity (kg/m·s)

c_p = heat capacity of corium (J/kg·K).

The direct use of such a correlation would result in large heat transfer at the wall, hence the no-crust approach usually includes the effect of a slug layer (Fig. 5a), which reduces the heat transfer across the concrete boundary. The slug HTC has never been measured; hence, generally a constant value is assumed. In this calculation, it was equal to 300 W/m^{2}K. The overall heat balance on the corium pool in ASTEC/MEDICIS is controlled by the heat transfer network assuming two different HTCs for the slag h_{slag} and the corium pool h_{conv} given by the BALI correlation. Hence, an effective HTC is defined as

$$h_{eff} = \frac{1}{\frac{1}{h_{conv}} + \frac{1}{h_{slag}}} \quad . \tag{2}$$

The MCCI model in AC2/COCOSYS is similar, but employs an even more simplified approach in which the effective HTC is not provided by Eq. (1), but provided as a constant input parameter. The latter approach assumes that $h_{slag} << h_{conv}$, so that the impact of h_{conv} may be neglected in Eq. (1). For AC2/COCOSYS, $h_{slag} = h_{eff}$, which is assumed to be 50 W/m^{2}K. Despite the MCCI model in COCOSYS being successfully validated versus experiments with oxidic corium using h_{eff} in the range of 100 to 300 W/m^{2}K, the reduced value of 50 W/m^{2}K was taken here since it is not possible to directly impose a heat flux at the top surface. Instead, the desired top surface heat flux was approximated in COCOSYS by a reduced h_{eff} value, resulting in elevated

TABLE V

Summary of Codes and Institutes Participating in the OECD/NEA ARC-F Project

Code Name	Institute	Crust Formation on the Concrete Interface
ASTEC/MEDICIS[14]	IRSN (France)	Not considered
TOLBIAC-ICB[15]	CEA (France)	Considered
AC2/COCOSYS[16]	GRS (Germany)	Not considered
MELCOR/CORQUENCH[17,18]	SNL (United States), CIEMAT (Spain), NRA (Japan)	Not considered

corium temperatures and elevated surface temperatures for radiation. Comparisons of these HTCs toward the concrete are presented in Fig. 4, where AC2/COCOSYS is indeed constant and MEDICIS HTC decreases from the value 300 W/m^{2}K to around 100 W/m^{2}K.

For TOLBIAC-ICB, a crust was assumed to exist at the interface between the corium and the concrete. Two model assumptions were available for the interface conditions. According to the first assumption, the interface could be in thermodynamic equilibrium with the corium pool (the so-called equilibrium crust model), where the pool/crust interface temperature is equal to the liquidus temperature at the pool composition and the composition of the crust increment is that of the solid in equilibrium with the corium pool composition.

The second available model assumes that the crust, which has the composition of the melt at the time at which it was solidifying (nonequilibrium stable crusts), remains stable and that the interface temperature is nevertheless at liquidus temperature.[23] What is important to stress is that both these physical assumptions impose an interface temperature equal to the liquidus temperature contrary to the other codes.

In TOLBIAC-ICB, the HTC at the pool/concrete interface is computed considering the convective heat flux from the pool at T_{pool} to the interface at $T_{liquidus}$ (whose convective lateral and vertical heat transfers are given by BALI correlations involving the concrete released gas superficial velocity[22]) and the released decay power inside the formed crust. As observed in Fig. 5, the order of magnitude of the bottom HTC obtained with TOLBIAC-ICB is in good agreement with the AC2/COCOSYS result, whereas the long-term lateral HTC value was closer to the ASTEC/MEDICIS value. It should be noted that the decay power in the crust was considered and had a great influence on the MCCI transient.

Indeed for a transient lasting several days with a pool solidifying, the crust thickness becomes large, incorporating most of the residual power, and this phenomenon is not negligible in the overall energy balance.[22,24] In TOLBIAC-ICB, the reduced temperature difference between the pool and the liquidus temperatures (compared to the other codes) was balanced by larger convective HTCs in the pool, as observed in Fig. 4b. The slag layer was not considered because the temperature at the concrete interface was the liquidus temperature, as presented in Fig. 6, so no solid could exist inside the pool.

The second model assumes a deviation from thermodynamic equilibrium (the so called nonequilibrium crust model) and considers a slag layer between the concrete and the crust, as in ASTEC/MEDICIS and AC2/COCOSYS, but as it is not the reference model, it was not considered in this benchmark. For the heat balance on the top surface, the computation was slightly more complicated, and it involved two cases presented in Figs. 5b and 5c. Initially, the crust did not exist in the codes ASTEC/MEDICIS and AC2/COCOSYS, and the heat flux was dependent on the upper convective HTC to the top surface and the temperature difference between the corium pool and the top surface T_{top}. However, in case T_{top} falls below the corium solidification temperature, a crust is formed, and the interface temperature T_{int} (between the pool and the crust) is assumed to be equal to this solidification temperature.

In AC2/COCOSYS the solidification temperature was assumed to be equal to the solidus temperature,

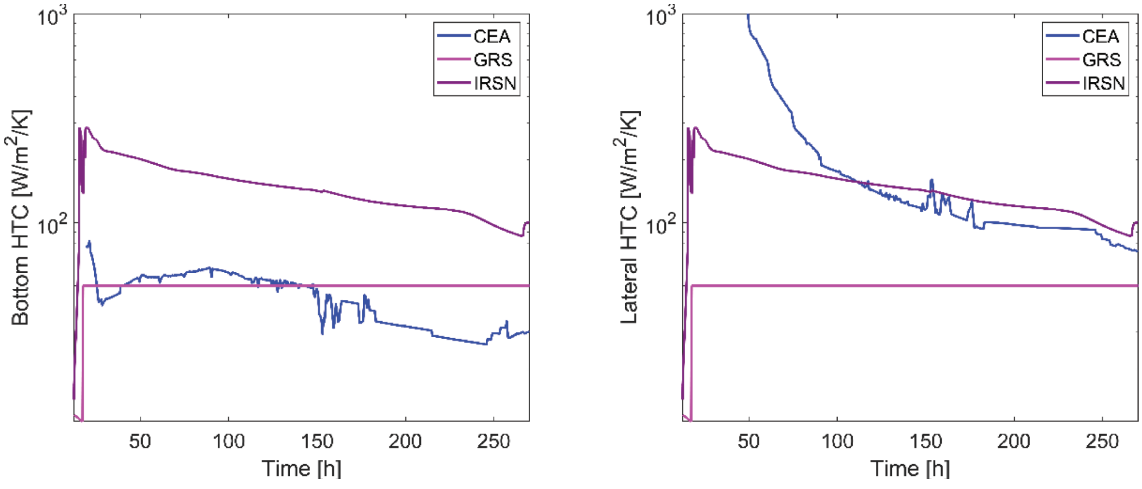

Fig. 4. (a) Bottom effective HTC and (b) lateral effective HTC.

whereas in MEDICIS the solidification temperature was evaluated between the pool liquidus and solidus temperatures according to the value of the threshold liquid volume fraction equal to 50%.

The MELCOR code had an approach similar to the one presented in AC2 and MEDICIS, however, details were not provided in the project.

In the TOLBIAC-ICB case, due to upper radiation and even more in case of water reflooding, a crust formed also at the upper corium pool surface. As already explained, these pool interfaces were at the liquidus temperature related to the pool composition (Fig. 6). One difference between TOLBIAC-ICB and the other codes is that in TOLBIAC-ICB, this crust existed from the beginning of the transient.

IV.B. Ablation Rate

The main result of the MCCI progression is represented by the ablation rates. This was also the variable of interest to investigate the reason for the unlimited erosion in the BSAF phase 2 results, which was the motivation for this exercise.

Depending on the modeling assumptions and the variables considered in the energy balances, the ablation rate models show differences. The ablation rate in MEDICIS and AC2 is presented in Eq. (3),

$$v_{ablation} = \frac{dx_{ablation}}{dt} = \frac{h_{eff}\left(T_{pool} - T_{ablation}\right)}{\Delta H_{abl}\rho_{s,conc}} \quad , \qquad (3)$$

where

h_{eff} = effective HTC in Eq. (1)

ΔH_{abl} = ablation concrete energy, defined as $\Delta H_{abl} = h_{conc}(T_{ablation}) - h_{conc}(T_0)$ with T_0 = 300 K [J/kg]

$h_{conc}(T_{ablation})$ = specific enthalpy of the concrete at $T_{ablation}$

$h_{conc}(T_0)$ = specific enthalpy of the concrete at T_0

$\rho_{s,conc}$ = density of the solid concrete at T_0 [kg/m^3].

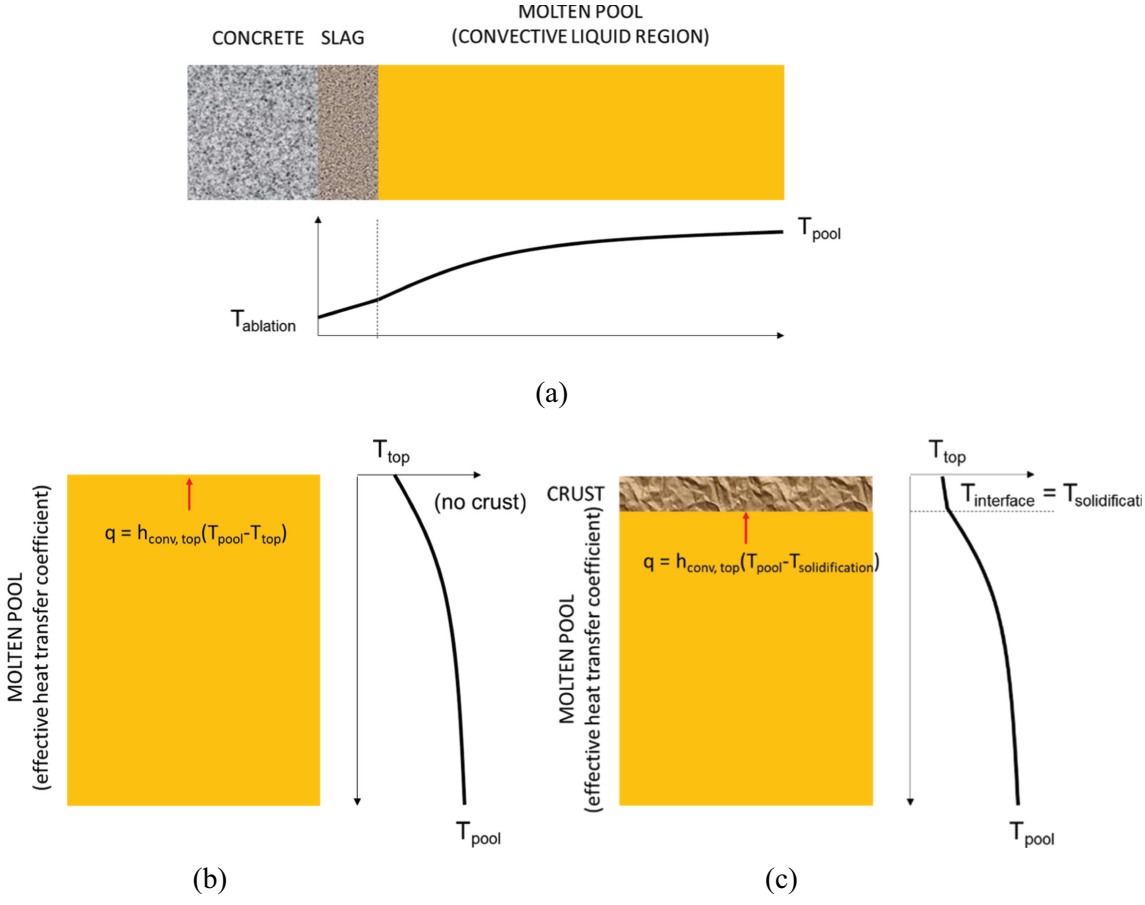

Fig. 5. Schematic view of the heat transfer network employed in the ASTEC/MEDICIS code and the COCOSYS/AC2 code: (a) heat balance on the concrete side and (b) and (c) two different states on the top surface.

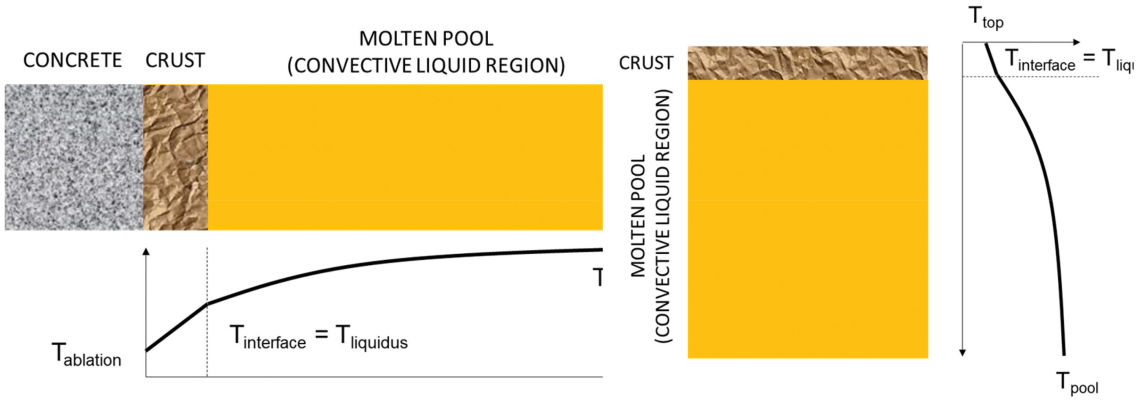

Fig. 6. Schematic view of the heat transfer network employed in the TOLBIAC-ICB code.

Hence the ablation energy provided in the exercise was effectively defined, including the heat increment and the latent heat of phase change.

On the other hand, the definition in TOLBIAC-ICB is expressed in Eq. (4),

$$v_{ablation} = \frac{dx_{ablation}}{dt} = \frac{\varphi_{towards\ concrete}}{\Delta H_{abl}\rho_{s,conc} + \rho_{l,conc}Cp_{l,conc}\left(T_{pool} - T_{abl}\right)} \quad . \tag{4}$$

This expression derives from an energy balance on a given volume of concrete whose enthalpy, receiving the heat flux $\varphi_{towards\ concrete}$ (W/m^2), evolves from $h_{conc}(T_0)$ at solid state to $h_{conc}(T_{pool})$ at liquid state. In Eq. (4), $\Delta H_{abl}\rho_{s,conc} = \rho_{s,conc}\left(h_{conc,solid}(T_{abl}) - h_{conc,solid}(T_0) + L\right)$, with L the enthalpy of phase change (J/kg). $\varphi_{towards\ concrete}$ gathers the heat flux released by the pool and the part released by the crust (owing to its decay power),

$$\varphi_{towards\ concrete} = h_{conv}\left(T_{pool} - T_{liquidus}\right) + \dddot{Q}\, e_{crust} \quad , \tag{5}$$

where

h_{conv} = convective HTC inside the pool

$T_{liquidus}$ = liquidus temperature at the pool composition

$\rho_{l,conc}$, $Cp_{l,conc}$ = density and specific heat of the liquid concrete, respectively

$\dddot{Q}$ = crust volumetric decay heat power (W/m^3)

e_{crust} = thickness of crust (m).

Different from Eq. (3), Eq. (4) employed by TOLBIAC-ICB considers the heat increment of the liquid concrete from the ablation temperature to the corium temperature when evaluating the energy balance on the pool (initially at T_{pool}) with the incoming molten concrete at $T_{ablation}$.

In MEDICIS and AC2, Eq. (3) is used to calculate the mass flux of the liquid and gaseous concrete decomposition products entering the melt layer at T_{abl}, and then the new melt layer temperature is iteratively solved for each time step, taking all mass and energy fluxes into and out of the melt layer into account.

V. COMPARISON OF RESULTS

Figure 7a presents the molten corium pool temperature evolution for all the codes. The corium pool temperature, whose initial value was about 1482 K, had an initial spike increase up to over 2600 K due to oxidations of the metals contained in the initial debris. Once the chemical reactions of the metals initially present in the corium ceased and the decay heat reduced, the temperature also reduced. It is noticeable that the temperature of the melt was always above the ablation temperature, i.e., 1541.0 K.

Considering Eq. (3), this result demonstrates why the erosion rate is always greater than zero, resulting in the unlimited erosion experienced in BASF phase 2 and in this exercise as well. The corium temperature evolution was relatively similar in all calculations, which asymptotically tended toward the ablation temperature, except for the TOLBIAC-ICB code in the CEA case, which can be attributed to the different boundary condition assumptions of the interface temperature at $T_{liquidus}$. The assumption that the interface temperature is equal to $T_{liquidus}$ indeed tends to generate a larger pool temperature.

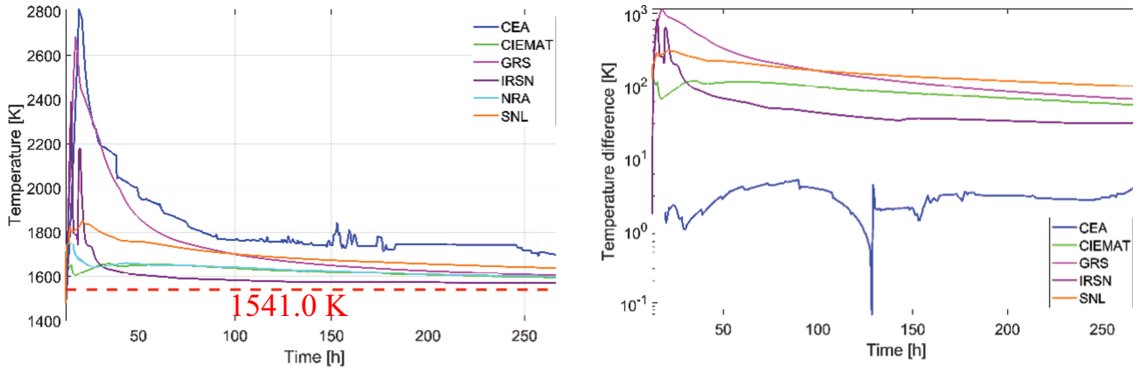

Fig. 7. Corium temperature variation: (a) whole temperature variation from 12.5 to 270 h and (b) temperature difference in Eq. (3) for all codes except for TOLBIAC-ICB, which used Eq. (4).

The temperature difference in Eq. (3), that is to say $T_{pool} - T_{ablation}$, is plotted in Fig. 7b for all codes, except for TOLBIAC-ICB, where $T_{pool} - T_{liquidus}$ is plotted according to Eq. (4). It is insightful from Fig. 7b that the temperature difference in TOLBIAC-ICB, which drives the ablation velocity, is around two orders of magnitude lower than in the other codes, but as already discussed, the HTC is larger in the TOLBIAC-ICB simulation than in the other codes.

Despite the corium pool temperature differences among some simulations, it is remarkable that the cavity erosion pattern, vertically and radially, is very similar among all the simulations, as presented in Fig. 8. This can be explained by the fact that the ablation rate is directly controlled by the flux to the concrete, which results from an energy balance over the pool. One exception is represented by the CIEMAT result, as it did not assume isotropic conditions. The same conclusion is supported by the ablation rate evolution presented in Fig. 9, which shows a very similar trend for all calculations.

This good agreement of the results, whatever the modeling assumptions adopted, implies that the major point controlling ablation is the energy balance on the corium pool and the distribution of heat fluxes (lateral, vertical), which have been assumed to be isotropic in this work.

Further investigation of the role of the crust could be expanded in the future, including a comparison with codes such as CORQUENCH,[25] where the option to consider the crust formation is included but with different assumptions for the solidification temperature, which is assumed to be the solidus point. Typical CORQUENCH results show that in the long term, the crust becomes thinner and thinner until its complete disappearance. This result depends on the assumption of the solidification or freezing temperature on the crust boundary. Indeed, with a concrete weight percent above 12%, the $T_{solidus}$ of the mixture drops below the decomposition temperature, creating the possibility for the crust to melt away in a long transient. Such a situation could not be generated with the assumption of solidification temperature equal to $T_{liquidus}$, as the temperature gradient across the crust would be always positive.

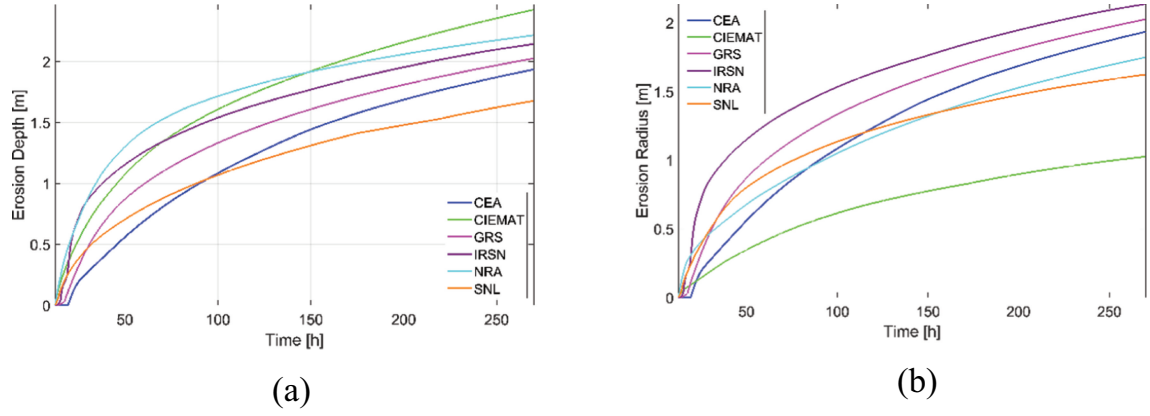

Fig. 8. Maximum concrete erosion (a) vertically and (b) radially.

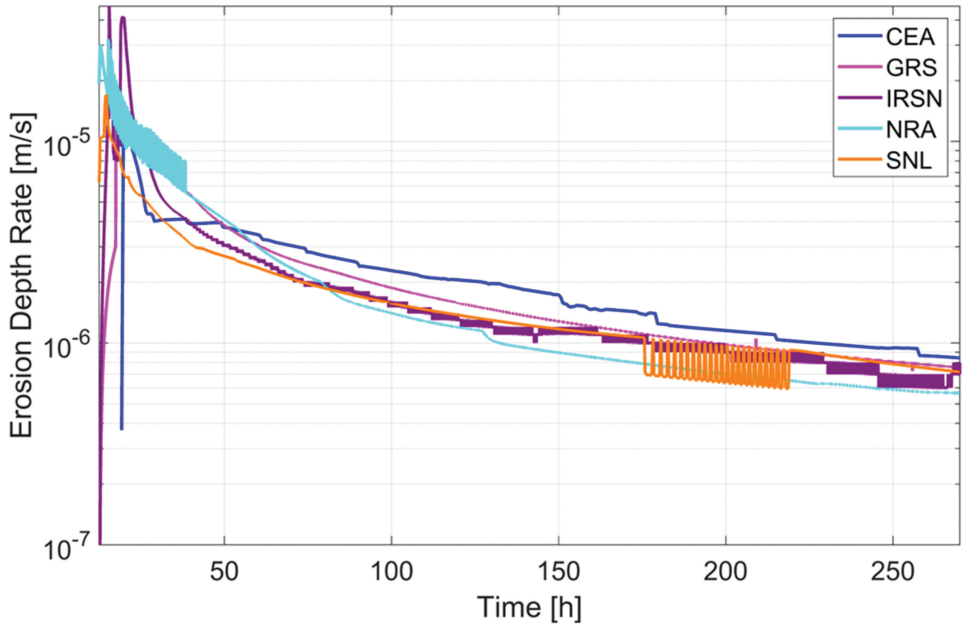

Fig. 9. Vertical ablation velocity.

The prediction of unlimited erosion is also clearly visible when plotting the total mass and the volume of eroded concrete presented in Fig. 10. In particular, a nonzero ablation rate (time derivative of the ablation depth) was observed on all calculations, even at $t = 270$ h. The total erosion mass was consistent among calculations showing a lower value, approximately half for CIEMAT, which assumed preferential side erosion.

The continuous erosion also affected the generation of ex-vessel hydrogen, which was estimated, based on the whole discussion, to be overpredicted. The overall generation is shown in Fig. 11a. In the figure, we noticed an initial larger trend in the generation, which was associated with the oxidation of metals like Zr that were present in the original discharged corium. Eventually the generation rate becomes similar for every code, except for CIEMAT, which showed consistently an almost half-generation rate. This hydrogen generation was associated with the persistent oxidation of continuously exposed rebar. In some calculations, such as CEA,

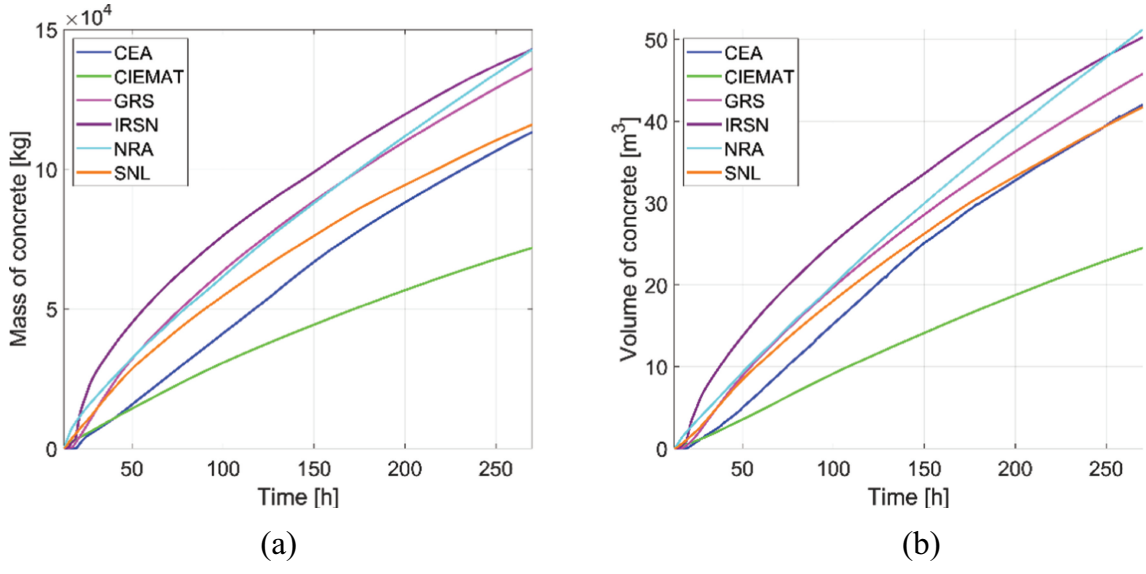

Fig. 10. (a) Mass of eroded concrete and (b) volume of eroded concrete.

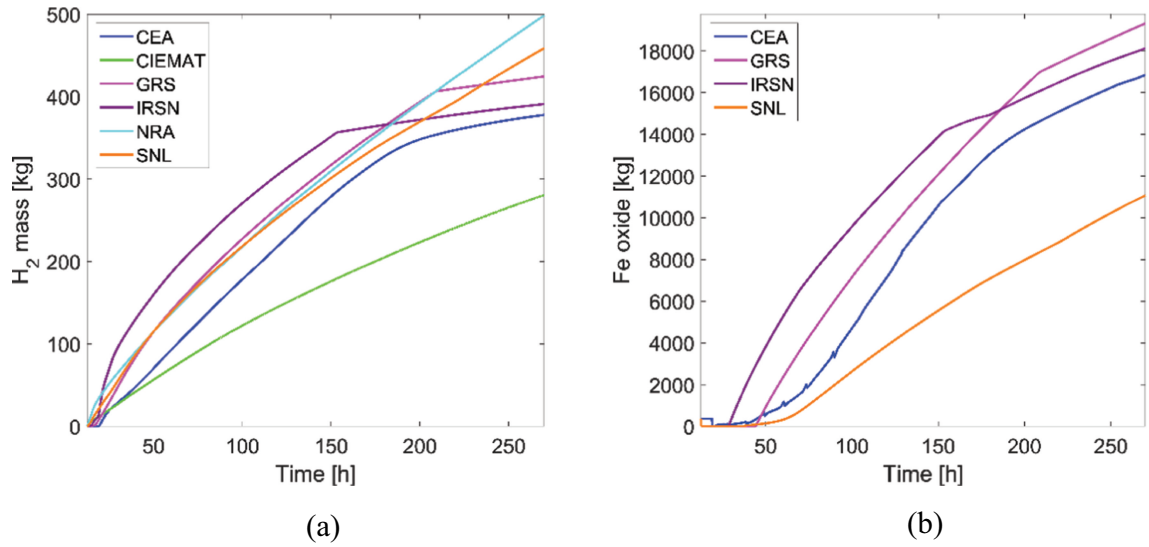

Fig. 11. (a) Hydrogen generation and (b) generation of iron oxide (including rebar).

GRS, and IRSN, the hydrogen generation reduced after around 150 to 200 h. This reduction was driven by the decreasing temperature, and hence, reduced Fe oxidation kinetics, as shown in Fig. 11b.

VI. DISCUSSION OF THE UNLIMITED EROSION

The results obtained in this benchmark demonstrated that a wide variety of lumped parameter codes dealing with MCCI will predict unlimited concrete erosion assuming the debris accumulating in the sump in dry conditions. From the heat balance point of view, this result could be simply explained by saying that the heat losses at the corium pool boundaries are always lower than the residual heat source in the pool represented by the decay heat. This condition leads the predicted ablation at 270 h, from the beginning of the accident, to exceed the size of the pedestal walls, as shown qualitatively in Fig. 12. Due to the tridimensionality of the pedestal internals, two pictures are presented. Figure 12a shows a cross section of the eroded area cutting between the two sumps. Figure 12b shows a circle of eroded concrete centered in the

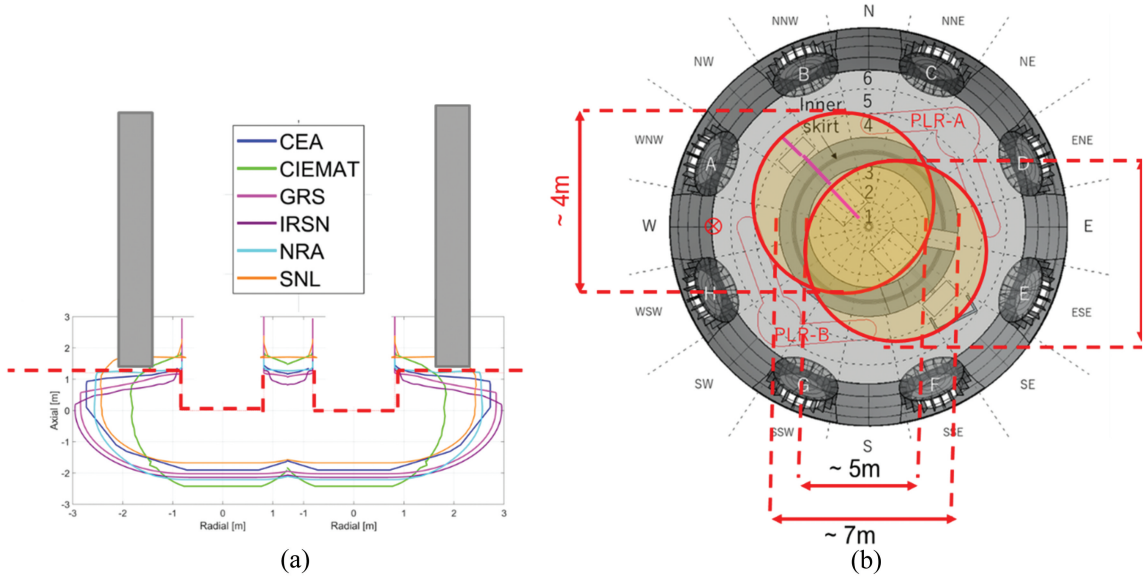

Fig. 12. (a) Cross section of the predicted erosion configuration in comparison with the pedestal walls and (b) top view of the predicted erosion around the sumps.

sump of a radius equal to the predicted value by the codes, around 2 m, as reported in Fig. 8. Figures 12a and 12b show that the prediction of all the codes would result in a pedestal wall not capable of supporting the whole reactor, which is conversely the evidence obtained by the internal inspections.

It was considered that there may be three contributions that need to be taken into deeper consideration for a more realistic simulation. First, the decay heat employed in the simulation (presented in Fig. 3) might be overpredicted, as debate still exists about the amount of semivolatile gases released from hot corium. Second, the heat losses from the surface might be larger than what we computed, in particular, in case the ablation temperature of the concrete was higher than what was assumed, maintaining a larger debris temperature. Finally, the heat losses to the concrete, at the moment considered adiabatic, might not be negligible in such a long transient and could represent a continuous heat sink to limit and eventually stop the erosion.

Work is ongoing to estimate the heat flux introduced by the consideration of the heat conduction through the concrete with online and offline modeling. Future work in the subsequent FACE (Fukushima Daiichi Nuclear Power Station Accident Information Collection and Evaluation) project of the OECD/NEA will address these three main uncertainties, which is to say, the initial decay heat in the debris, the decomposition temperature and energy, and the heat losses due to conduction in the concrete.

VII. CONCLUSION

The present work provided interesting insights into MCCI modeling in SA codes. The most significant ones are highlighted here:

1. The results of the main parameters were very consistent between the codes once the same boundary conditions and initial conditions were provided.

2. The erosion and ablation rates were modeled consistently in the different codes considered in this benchmark, despite some observable differences.

3. Assuming a crust formation between the molten materials and concrete, for example, does affect the temperature of the molten pool, but it does not significantly affect the final concrete erosion magnitude.

4. Given the models' validation against the available database, the continuous erosion indicated that in the long run (no experiments have addressed times as long as those in Fukushima Daiichi), the models included in this investigation did not capture the balance between heat losses and decay heat that the evidence indicated.

5. It is worth noting that, beyond erosion depth, this deviation in the long-term behavior of MCCI models might influence other aspects, such as combustible gas production or FP release. However, given that it is postulated that this would be a long-run effect, neither the PCV atmosphere composition nor the potential source term would be heavily changed in the short term.

According to the these highlights, three main points have been identified for future investigation: (1) the overall decay heat, (2) the concrete decomposition temperature and associated energy, and (3) the heat flux due to conduction through concrete. Work is ongoing in a subsequent project to the OECD/NEA ARC-F to consider each of these issues through sensitivity analyses.

Disclosure Statement

No potential conflict of interest was reported by the authors.

ORCID

Marco Pellegrini http://orcid.org/0000-0002-6656-2175

References

1. M. PELLEGRINI et al., "Main Findings, Remaining Uncertainties and Lessons Learned from the OECD/NEA BSAF Project," *Nucl. Technol.*, **206**, *9*, 1449 (2020); https://doi.org/10.1080/00295450.2020.1724731.

2. L. E. HERRANZ et al., "Overview and Outcomes of the OECD/NEA Benchmark Study of the Accident at the Fukushima Daiichi NPS (BSAF) Phase 2—Results of Severe Accident Analyses for Unit 1," *Nucl. Eng. Des.*, **369**, 110849 (2020); https://doi.org/10.1016/j.nucengdes.2020.110849.

3. M. SONNENKALB et al., "Overview and Outcomes of the OECD/NEA Benchmark Study of the Accident at the Fukushima Daiichi NPS (BSAF), Phase 2—Results of Severe Accident Analyses for Unit 2," *Nucl. Eng. Des.*, **369**, 110840 (2020); https://doi.org/10.1016/j.nucengdes.2020.110840.

4. T. LIND et al., "Overview and Outcomes of the OECD/NEA Benchmark Study of the Accident at the Fukushima Daiichi NPS (BSAF), Phase 2—Results of Severe Accident Analyses for Unit 3," *Nucl. Eng. Des.*, **376**, 111138 (2021); https://doi.org/10.1016/j.nucengdes.2021.111138.

5. "2022.2.8 Implementation Status of the Unit 1 Primary Containment Vessel Internal Investigation (from Investigation on February 8) at the Fukushima Daiichi

Nuclear Power Station," Tokyo Electric Power Company Holdings, Inc. (2024); https://www4.tepco.co.jp/en/news/library/archive-e.html?video_uuid=j295y47o&catid=61785 (current as of Jan. 1, 2024).

6. "2022.2.9 Implementation Status of the Unit 1 Primary Containment Vessel Internal Investigation (from Investigation on February 9) at the Fukushima Daiichi Nuclear Power Station," Tokyo Electric Power Company Holdings, Inc. (2024); https://www4.tepco.co.jp/en/news/library/archive-e.html?video_uuid=hjo1v4ul&catid=61785 (accessed Jan. 1, 2024).
7. "2022.03.24 Implementation Status of Unit 1 Primary Containment Vessel Internal Investigation (ROV-A2) (Work Conducted Between March 14~16) at the Fukushima Daiichi Nuclear Power Station," Tokyo Electric Power Company Holdings, Inc. (2024); https://www4.tepco.co.jp/en/news/library/archive-e.html?video_uuid=yw0uzql2&catid=61785 (accessed Jan. 1, 2024).
8. "2022.05.23 Implementation Status of the Unit 1 Primary Containment Vessel (PCV) Internal Investigation (ROV-A2) (Work Conducted Between May 17~19)," Tokyo Electric Power Company Holdings, Inc. (2024); https://www4.tepco.co.jp/en/news/library/archive-e.html?video_uuid=sd7bw090&catid=61785 (accessed Jan. 1, 2024).
9. "2023.04.04 Implementation Status of the Unit 1 Primary Containment Vessel (PCV) Internal Investigation (ROV-A2) (Work Conducted Between March 28~30, 2023)," Tokyo Electric Power Company Holdings, Inc. (2024); https://www4.tepco.co.jp/en/news/library/archive-e.html?video_uuid=14952&catid=61785 (accessed Jan. 1, 2024).
10. D. L. LUXAT et al., "MAAP-MELCOR Crosswalk Phase 1 Study," *Nucl. Technol.*, **196**, *3*, 684 (2016); https://doi.org/10.13182/NT16-57.
11. "Evaluation into the Amounts of Water Injected to Unit 1 by Fire Engines," TEPCO progress report, Attachment 1-5 (2017); https://www.tepco.co.jp/en/press/corp-com/release/betu17_e/images/171225e0212.pdf.
12. PELLEGRINI et al., "Benchmark Study of the Accident at the Fukushima Daiichi Nuclear Power Plant (BSAF Project)—Phase I Summary Report," p. 27, Nuclear Energy Agency (Mar. 2015), https://www.oecd-nea.org/upload/docs/application/pdf/2021-02/csni-r2015-18.pdf.
13. "OECD/NEA State of the Art Report on Molten Corium Concrete Interaction and Ex-Vessel Molten Core Coolability." Nuclear Energy Agency (2017).
14. M. CRANGA et al., "The MEDICIS Code, a Versatile Tool for MCCI Modelling," *Proc. Int. Congress on Advances in Nuclear Power Plants* (*ICAPP'05*), **4**, 2167 (2005).
15. B. SPINDLER, B. TOURNIAIRE, and J. M. SEILER, "Simulation of MCCI with the TOLBIAC-ICB Code Based on the Phase Segregation Model," *Nucl. Eng. Des.*, **236**, *19–21*, 2264 (2005); https://doi.org/10.1016/j.nucengdes.2006.03.023.
16. C. SPENGLER et al., "Uncertainty and Sensitivity Analyses in Support of Model Development and Validation of the Containment Module COCOSYS of the AC2 Code—Application for Molten Corium/Concrete Interaction (MCCI)," presented at the 12th Int. Topl. Mtg. on Nuclear Reactor Thermal-Hydraulics (NUTHOS-12) (2018).
17. L. L. HUMPHRIES et al., "MELCOR Computer Code Manuals. Vol. 1: Primer and Users' Guide Version 2.1.6840," SAND2015-6691R, Sandia National Laboratories (2015).
18. L. L. HUMPHRIES et al., "MELCOR Computer Code Manuals. Vol. 2: Reference Manual. Version 2.1.6840," SAND2015-6691R, Sandia National Laboratories (2015).
19. V. BOUYER et al., "In Large Scale Vulcano MCCI Test Considering 1F Condition," presented at the European Review Mtg. on Severe Accident Research (ERMSAR 2019), p. 107, Prague, Czech Republic, March 2019.
20. S. BAKARDJIEVA et al., "Improvement of the European Thermodynamic Database NUCLEA," *Prog. Nucl. Energy*, **52**, *1*, 84 (2010); https://doi.org/10.1016/j.pnucene.2009.09.014.
21. J.-M. BONNET, "Thermal Hydraulic Phenomena in Corium Pools for Ex-Vessel Situations: The BALI Experiment," presented at the OECD Workshop on Ex-vessel Coolability (FZKA 64753), Karlsrühe, Germany, 1999.
22. J.-M. BONNET, "Thermal Hydraulic Phenomena in Corium Pools for Ex-Vessel Situations: The BALI Experiment," presented at ICONE8, Baltimore, Maryland, 2000.
23. M. GANGA et al., "Towards an European Consensus on Possible Causes of MCCI Ablation Anisotropy in an Oxidic Pool," *Ann. Nucl. Energy*, **74**, 72 (2014); https://doi.org/10.1016/j.anucene.2014.07.017.
24. N. SEILER, C. JOURNEAU, and M. PELLEGRINI, "Advanced Analyses of Molten Core Corium Interaction with TOLBIAC-ICB at Fukushima Daiichi Unit 1 in the Framework of the ARC-F Project," presented at the Int. Topl. Workshop on Fukushima (FDR2022-1070), and the Int. Topl. Workshop on Fukushima Decommissioning Research, J-Village, Naraha, Fukushima, Japan, Oct 14–16, 2022.
25. M. T. FARMER, "The CORQUENCH Code for Modeling of Ex-Vessel Corium Coolability Under Top Flooding Conditions: Code Manual-Version 4.1-Beta," ANL-18/22, Argonne National Laboratory (Aug. 2018); https://publications.anl.gov/anlpubs/2018/10/146345.pdf.
26. PELLEGRINI et al., "Benchmark Study of the Accident at the Fukushima Daiichi Nuclear Power Plant—Summary Report," p. 20, Nuclear Energy Agency (2021); https://www.oecd-nea.org/upload/docs/application/pdf/2021-09/7525_bsaf.pdf.